

Adaptive Modeling of Correlated Noise in Space-Based Gravitational Wave Detectors

Ya-Nan Li, Yi-Ming Hu, En-Kun Li

E-mail: lienk@mail.sysu.edu.cn

MOE Key Laboratory of TianQin Mission, TianQin Research Center for Gravitational Physics & School of Physics and Astronomy, Frontiers Science Center for TianQin, Gravitational Wave Research Center of CNSA, Sun Yat-sen University (Zhuhai Campus), Zhuhai 519082, People's Republic of China

18 April 2025

Abstract. Accurately estimating the statistical properties of noise is important in space-based gravitational wave data analysis. Traditional methods often assume uncorrelated noise or impose restrictive parametric forms on cross-channel correlations, which could lead to biased estimation in complex instrumental noise. This paper introduces a spline-based framework with trans-dimensional Bayesian inference to reconstruct the full noise covariance matrix, including frequency-dependent auto- and cross-power spectral densities, without prior assumptions on noise shapes. The developed software **NOISAR** can recover the features of the noise power spectrum curves with a relative error $\leq 10\%$ for both auto- and cross-one.

1. Introduction

Ground-based gravitational wave (GW) observatories, such as LIGO [1], Virgo [2], KAGRA [3], and the upcoming space-based detectors, such as TianQin [4, 5], Laser Interferometer Space Antenna (LISA) [6], and Taiji [7], are designed to detect extremely weak signals from astrophysical and cosmological sources [8]. These signals are often buried in instrumental noise originating from test-mass (TM) acceleration noise, optical metrology system (OMS) noise, and laser frequency noise [5, 9, 10]. Although laser frequency noise can be suppressed by applying the time-delay interferometry (TDI) method [11–13], the other two kinds remain in the data and will influence the parameter estimation precision of GW signals. Accurate characterization and modeling of the noise are critical for distinguishing between noise and genuine GW signals, especially for stochastic gravitational wave backgrounds (SGWBs) [14–17], which are inherently weak and diffuse.

Space-based detectors are expected to detect GWs from different kinds of sources in the millihertz frequency band, e.g., ultracompact binaries (UCBs), binary black holes (BBHs), et al. The signals provide constraints on the origin and evolution of compact binaries and the structure of the Milky Way [18, 19]. Sensitive detection and accurate

parameter estimation of the GW signals are thus important for us when exploring the rich information. A fundamental challenge in GW data analysis for space-based detector is mainly due to the large amount (tens of thousands) and long duration of detectable signals, which overlap in both time and frequency domain. To simultaneously recover all resolvable signals in the data stream with noise and eliminate the cumulative error of hierarchical fit, people apply a global fit for all kinds of sources and noise [20–23]. In global analysis, an essential step is the reconstruction of the unknown noise properties, for Gaussian noise shown as a noise covariance matrix, whose diagonal elements are the variance of each parameter, and the off-diagonal ones are the covariance between different parameters.

To eliminate laser frequency noise, which is much stronger than GW signals, the TDI method is applied to the data processing [11–13]. Michelson combinations type of TDI channels, e.g., X , Y , Z , contain highly correlated noises. Quasi-uncorrelated TDI channels A , E , and T are orthogonal (or uncorrelated) under equal-arm length and identical instrument noise assumptions. To simplify complex parameter estimation problems, most studies consider utilizing quasi-orthogonal A , E , and T channel data by assuming that the noise covariance matrix is diagonal. However, in real cases, the armlength and instrument noises are hardly equal, which means that the off-diagonal elements in the noise covariance matrix cannot be omitted. In global analysis pipelines where signals from various types of sources and noise are alternately updated, a more complete noise modeling would benefit more accurate parameter estimation [20–23]. Therefore, to avoid the bias in parameter estimation of GW signals caused by those factors, the full covariance matrix of different channels needs to be estimated.

So far, some researchers in the field of SGWB have considered relatively comprehensive modeling of noise since correlated noise could mimic or obscure the SGWB signals and significantly affect the ability to detect them [17]. Adams et al. [24] distinguish between SGWB and instrumental noise while the full noise covariance matrix is taken into account, with each element derived from known analytical expressions. Baghi et al. [25] develop a Bayesian framework using cubic splines to model instrumental noise of unknown spectral shape for LISA, enabling robust detection of SGWBs without prior assumptions on noise characteristics. In their work, they assumed the laser frequency noise is fully suppressed by the time-delay interferometry (TDI), thus they ignored the laser noises and assumed no correlations between single-link measurements and also a fixed TDI transfer function matrix. Caporali et al. [26] study the impact of correlated noise on SGWB detection and relative parameter estimation for the next generation ground-based GW interferometer Einstein Telescope (ET) [27, 28]. They perform a Bayesian analysis on simulated data and illustrate that neglecting correlated noise leads to significant biases in the parameter reconstruction of SGWB.

Multiple kinds of methods have been developed for noise reconstruction. The typical **Welch** method [29] median averages the power spectrum of “off-source” data segments near a candidate signal, which can be biased due to drifts in noise levels and noise transients [30–32]. Due to these reasons, “on-source” spectral estimation methods

Bayesline/Bayeswave are developed. They combine a cubic spline for broadband noise and different models for narrowband noise, considering the multi-component and variable dimension, leveraging the advantage of trans-dimensional Bayesian method [33, 34]. These two methods have been proven to perform well in recovering auto-correlated noise power spectra for both ground-based and space-based gravitational wave detectors [35–37].

In this paper, we aim to develop a pipeline **NOISAR** (NOIse Space Adaptive Reconstruction), to reconstruct the full noise covariance matrix including correlated components for space-based GW detectors, which can be integrated into parameter estimation pipelines for various signals, such as global analysis. Our method combines spline interpolation with a trigonometric function expression to semi-analytically fit both the Power Spectral Density (PSD) and the Cross Spectral Density (CSD) between different channels. This method is a phenomenological approach and does not rely on any prior knowledge about the noise model, which implies that users only need to provide the noise data (for example, data stream after subtracting bright signals and cleaning glitches), and get the noise reconstruction after running the pipeline. It is expected to be an important part of global data analysis, updating noise model in each iteration and improving the accuracy of parameter estimation for all kinds of sources. It should be noted that the current pipeline developed in this study is a preliminary version, designed for modeling pure Gaussian and stationary instrumental noise. This method has potential for handling foreground noise composed of unresolvable sources, because it is phenomenological, and the shape of the PSD curve resulting from the combined effects of foreground noise and instrumental noise can also be recovered. However, this work does not yet address more complex scenarios such as data gaps, transient noise in data stream, or non-stationary noise. These aspects will be considered in the future advanced NOISAR framework. In this paper, as a simple case, we show an example of fitting PSD and CSD for Gaussian and stationary instrument noise.

The following is the outline of this paper. Sec.2 introduces the theoretical noise power spectra of TianQin detectors in the X , Y , and Z channels. Sec.3 describes in detail the methods used in this study, including noise modeling and the Bayesian inference approach. Sec.4 shows the PSD and CSD fitting results compared with theoretical ones. Sec.5 gives a conclusion of this work and discusses the scope of the application and future development of this method.

2. Instrument Noise In Detector Channels

Different TDI channels are defined as linear combinations of time-shifted single-link components. Here we consider the X , Y , and Z TDI channels, which are correlated with each other whenever the arm lengths are equal.

Assuming that the instruments are all the same, one has the analytical formula of PSD and CSD for X , Y , and Z channels [11]:

$$S_X^n = 16 \sin^2 u [S_s + 2(1 + \cos^2 u)S_a], \quad (1)$$

$$S_{XY}^n = -8 \sin^2 u \cos u [S_s + 4S_a]. \quad (2)$$

where $u = 2\pi fL/c$, with light speed c and TianQin detector arm length $L \approx 1.7 \times 10^8 \text{m}$ for TianQin. S_a and S_s are test-mass acceleration and readout noise (mainly shot noise). The PSD of test-mass acceleration noise for TianQin is given by

$$S_a(f) = \frac{N_a}{(2\pi fc)^2} \left(1 + \frac{0.1 \text{mHz}}{f}\right). \quad (3)$$

where $\sqrt{N_a} = 3 \times 10^{-15} \text{m/s}^2 \text{Hz}^{-1/2}$ is the designed requirement for acceleration noise. For TianQin, the readout noise PSD is

$$S_s(f) = N_s \left(\frac{2\pi f}{c}\right)^2, \quad (4)$$

where $\sqrt{N_s} = 1 \text{pm Hz}^{-1/2}$ [5].

FIG. 1 shows the PSD and absolute value of CSD in logarithmic coordinates over frequency. To simulate more realistic noise, whose PSD curve is not so ideally flat in the low frequency region, we add a small disturbance on top of the theoretical PSD. The averaged fluctuation in the whole frequency region is $\sim 3\%$ theoretical PSD, and the maximum fluctuation point is about twice the theoretical PSD.

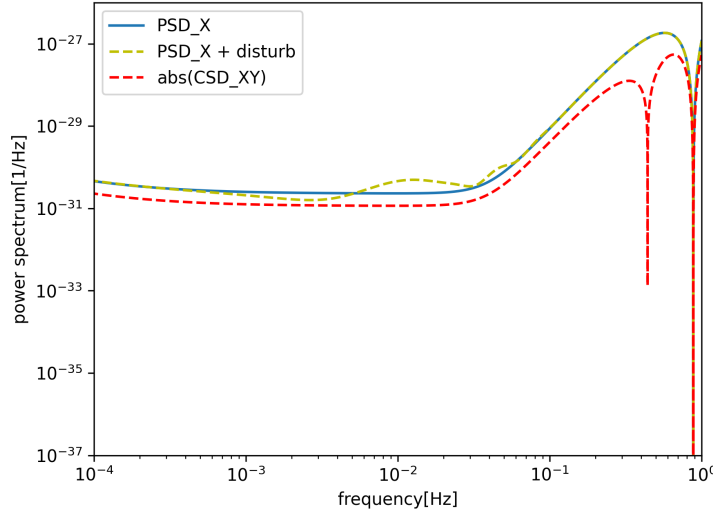


Figure 1: Analytical PSD (blue solid) and absolute value of CSD (red dashed). Disturbed PSD is shown as a yellow dashed line.

Notice that there is a descending peak in PSD curve and two peaks in CSD curve. The peak at the higher frequency, which both PSD and CSD have, is obtained by the spectrum values transitioning from positive to zero. It's mathematically due to the $\sin^2(f/f^*)$ in detector response functions, where $f^* \equiv c/2\pi L$ is the “transfer frequency”. The other peak results from the CSD crossing the zero point from negative values to positive values, due to the $\cos(f/f^*)$ term. We also aim to accurately fit these important features.

We notice that under the ideal assumptions, i.e., equal armlength and identical noises, the generation of correlated instrumental noise in XYZ channels can be done assuming that $S_X = S_Y = S_Z$ and $S_{XY} = S_{XZ} = S_{YZ}$. However, this assumption is not necessary and our method can apply to more general cases. The details of data generation are described in the following section.

3. Methodology

3.1. Preprocessing Phase

We generate correlated noise data $n(f)$ using the frequency-dependent noise covariance matrix $\mathbf{C}(f)$. The diagonal elements of $\mathbf{C}(f)$ are the auto-PSDs of X , Y , and Z channels, and the off-diagonal elements are CSDs between each two different channels. In real scenarios, if the detected data is in the time domain, first Fourier transforms it into the frequency domain since the PSD and CSD estimation is performed in the frequency domain in this method.

In this section, we aim to smooth the raw data and get an initially averaged spectrum according to the definition of covariance:

$$\text{Cov}(X(t), Y(t)) = \langle (X(t) - \langle X(t) \rangle)(Y(t) - \langle Y(t) \rangle) \rangle, \quad (5)$$

$$= \frac{1}{n} \sum_{i=1}^n (X(t_i) - \langle X(t) \rangle)(Y(t_i) - \langle Y(t) \rangle). \quad (6)$$

where $X(t)$ and $Y(t)$ represent the time domain data in channel X and Y , $X(t_i)$ and $Y(t_i)$ are the i th points in $X(t)$ and $Y(t)$ with total data point number n . $\langle \cdot \rangle$ denotes the expectation value.

In frequency domain, the variance and covariance become:

$$\text{PSD} = 2 \langle \tilde{n}_X(f) \tilde{n}_X^*(f') \rangle / \delta(f - f'), \quad (7)$$

$$\text{CSD} = 2 \langle \tilde{n}_X(f) \tilde{n}_Y^*(f') \rangle / \delta(f - f'). \quad (8)$$

where $\tilde{n}_X(f)$ and $\tilde{n}_Y(f)$ are frequency domain data after the Fourier transform, and the asterisk denotes the complex conjugate. $\delta(f - f')$ represents a differential element in frequency region. The expectation value is calculated by averaging over n data points:

$$\langle \tilde{n}_X(f) \tilde{n}_X^*(f') \rangle = \frac{1}{n} \sum_{i=1}^n (\tilde{n}_X(f) \tilde{n}_X^*(f')) \quad (9)$$

$$\langle \tilde{n}_X(f) \tilde{n}_Y^*(f') \rangle = \frac{1}{n} \sum_{i=1}^n (\tilde{n}_X(f) \tilde{n}_Y^*(f')) \quad (10)$$

In reality, instead of averaging directly by Eq. (9) and (10), we take the median among every n points, to avoid the influence of outliers that deviate too far from the mean value on the calculation of the average. Then we get initial median smooth spectra D_X and D_{XY} . Those spectrums, derived only from the data, already provide a relatively comprehensive description of the noise characteristics, however, with strong random fluctuations that prevent them from serving as a universal representation of the

features. It is necessary to smooth it out to serve as a noise model. The noise modeling method described in the following sections is based on those median smooth spectra. In this work, we fit the real part of CSD since the imaginary part is small in magnitude and fluctuates around zero.

3.2. Modeling the noise covariance matrix

3.2.1. Spline Parameterization In theory, expressing an unknown function in the form of an N -degree polynomial allows for the derivation of the functional relationship between the independent and dependent variables by obtaining its coefficient matrix. Here, the polynomial can be written as:

$$S = \sum_{i=0}^N a_i (f - f_i)^i \quad (11)$$

where S represents the fitted model, N is the degree of the polynomial expansion, and a_i is the coefficient to be estimated. The calculation of an N -degree matrix is time-consuming. In practice, we use the spline interpolation method to model the complete curve with only tens or hundreds of knots. We choose the B-spline-based `Python` interpolation package *make_interp_spline* to avoid the large oscillations between knots in cubic spline curves, and the interpolated curve will pass through each knot. Due to the noise data spanning multiple orders of magnitude, direct interpolation yields poor results. Therefore, the data is first log-transformed to interpolate smoothly within the same order of magnitude and then converted back to the original scale. Since negative values exist in the CSD, directly taking the logarithm is not feasible. Instead, we employ a segmented approach involving taking the logarithm of the absolute values and then restoring the signs. Detailed descriptions of this method are provided in Sec.3.3.

The initial knots are picked from the log-transformed median smooth spectrum PSD_0 and CSD_0 we've got in previous steps, in the logarithmic frequency region below 20mHz. Here we simply choose 40 knots log-uniformly in this region. The number 40 is decided by several rounds of trials, so it's not a mandatory choice. The log-uniform choice is justified because, in our case, we consider pure Gaussian noise whose spectral density exhibits a simple and smooth profile in the low-frequency region. In more complex cases, e.g., there are non-stationary noise, residual glitches, or data gaps in the data stream, a more data-driven knot selection approach may need to be considered. For example, average the data on different orders (i.e., average over every 32 points and over 64 points) and get two average-smoothed curves. Knots should be picked at locations where the difference between two curves exceeds a certain threshold. Notice that in the high-frequency region (where $f > 20\text{mHz}$) the PSD and CSD exhibit a drop to zero mathematically due to the $\sin^2(f/f^*)$ term, and the CSD passes through zero at a certain point due to the $\cos(f/f^*)$ term. To recover the features, we choose more knots linearly near the zeros. Here we set about 10 knots in the region surrounding each zero point. The width of each region is $\sim 0.05\text{Hz}$. The number of knots is also chosen empirically.

FIG. 2 shows the initial log-transformed median smooth spectra with blue lines, knots with yellow dots, and the spline curve with black lines. To observe the interpolation results near the zeros, we show a zoomed-in view of the high-frequency region in a subplot, and present it on a linear horizontal axis. The figure shows that spline interpolation does not fit the characteristic well, where the curve drops to zero. Besides, since there are a lot of cross-zero points in correlated data, spline interpolation may lead to more than one cross-zero feature in the recovered CSD curve, different from the theoretically expected result which has only one. To deal with the problems, we consider a semi-analytic noise model, combining spline interpolation for phenomenological fitting and a trigonometric function (described in Sec.3.2.2) to reproduce the sharp drop features in the high-frequency region.

3.2.2. Trigonometric Function As mentioned before, we use trigonometric functions to recover the power spectrum near zero points:

$$h_{PSD}(f) = A_{PSD}(f) \sin^2(2\pi f/f^*), \quad (12)$$

$$h_{CSD}(f) = A_{CSD}(f) \sin^2(2\pi f/f^*) \cos(2\pi f/f^*). \quad (13)$$

$A(f)$ is a polynomial function of f with multiple power terms. Empirically, a cubic term (f^3) as the highest order suffices for TianQin PSD and CSD fitting requirements, i.e., $A(f) = af^3 + bf^2 + cf + d$. The coefficients a, b, c, d are the parameters we want to fit in the following Bayesian analysis process. The zero-crossing point is caused by the $\cos(2\pi f/f^*)$ term, thus, this term only appears in Eq.(13) for CSD fitting. Note that here we do not vary the coefficients in sin and cos terms. This implies an underlying assumption that the detector's three arms are of equal length, thus, hold for the first generation TDI. In the second generation TDI scenario, coefficients of those two terms require subsequent fitting through Bayesian analysis.

The frequency band where the spline interpolation curve is replaced by a trigonometric function depends on where the zero points are in the data. Theoretical CSD of TianQin has only one cross-zero point below 1Hz, but the generated data and the initial smoothed spectrum D_{XY} have a lot of such points, see the blue line in the right panel of FIG. 2. Direct interpolation would lead to more than one cross-zero point in the CSD curve, which is not what we expect. Thus, the frequency band covering all those points is where we adopt the trigonometric function to fit CSD. Additionally, another sub-band that covers the second zero point that appears in both PSD and CSD has been set with a width of ~ 4 mHz. This is an entirely artificial and empirical choice, using the trigonometric function to fit the peak only within a very small range near the zero point.

We combine the B-spline interpolation and the trigonometric function to fit the whole spectrum curve. An important issue is how to make sure the transition boundary is smooth between the two parts. In this study, the criterion for determining smoothness is whether the relative difference between the spline interpolation value (S_{spline}) and the trigonometric function value (S_{trig}) at the connection point, calculated

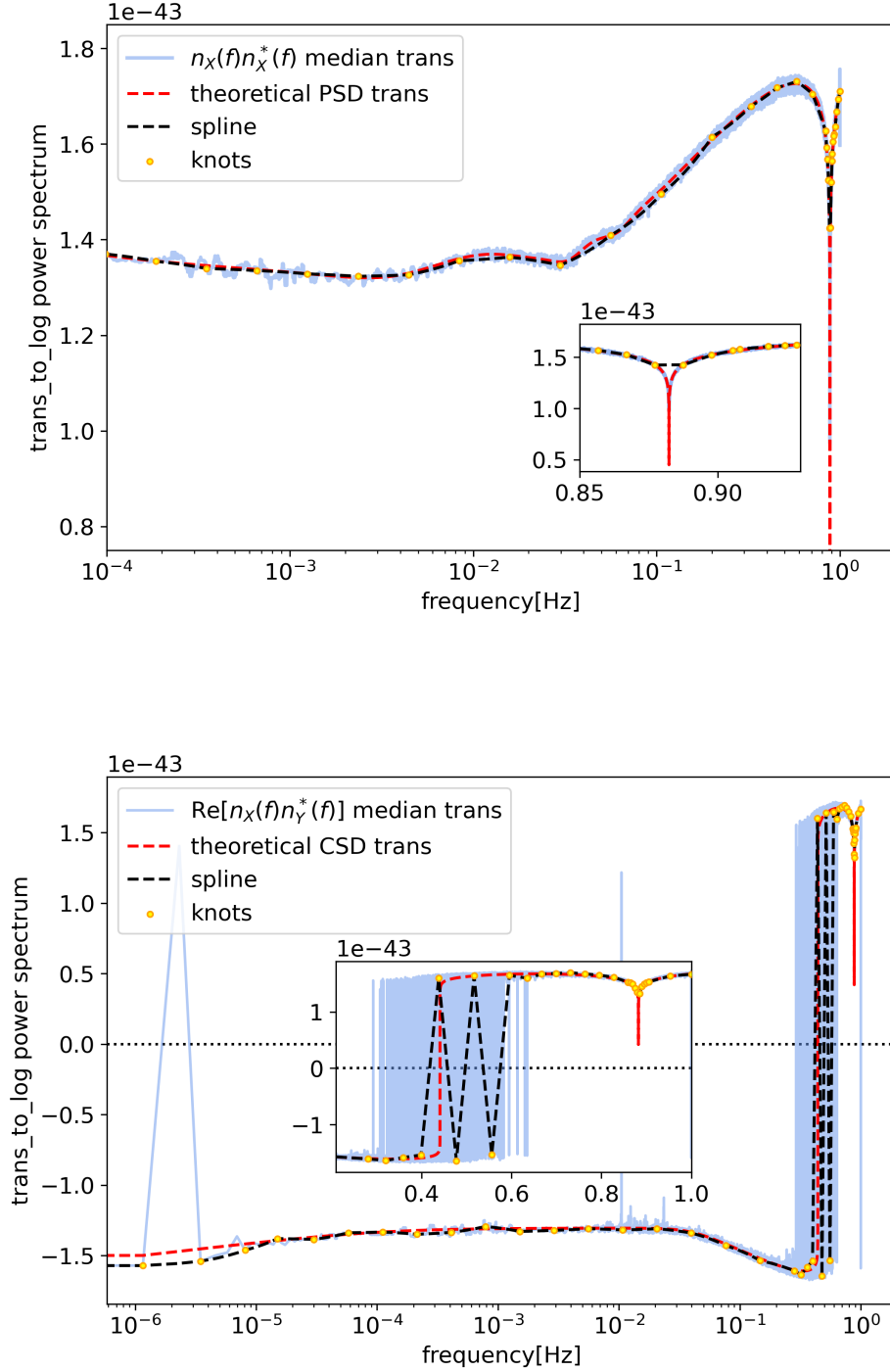


Figure 2: Median estimate for the spectrum after log-transforming (blue) and the initial spline (dashed black) on a logarithmic frequency x-axis, and with a subplot on a linear x-axis. The subplot shows a zoomed-in view of the high-frequency region. The yellow dots are knots picked from the median data spectrum, and the interpolation curve passes through these points. The upper panel shows results from single-channel data, and the bottom panel shows results from correlated data.

by $|(S_{trig} - S_{spline})/S_{spline}|$, is smaller than a predefined threshold. Here, the “connection point” means the point in the frequency region which is the boundary of two modeling methods. In this paper, the threshold is artificially set to 10%. And the initial coefficient values $a_{ini}, b_{ini}, c_{ini}, d_{ini}$ are chosen according to this criterion too. A lower threshold can improve smoothness at the connection point, but may reduce the acceptance rate in subsequent Bayesian updates.

3.3. Logarithmic method of the data

This section aims to transform the initial average smoothed spectrum into logarithmic form, to enable spline interpolation at the same order of magnitude and obtain smooth curves.

For correlated noise data, the cross-spectrum density contains both positive and negative values, thus, directly taking the logarithm is infeasible. To deal with this problem, we segment the spectrum into three parts based on its sign and magnitude: positive part (named “+”), negative part (named “-”), and a transition part near zero. For the points with values within a small range around 0 (with S_{th} as the boundary, S_{th} is chosen artificially and will be described below), retain their original sizes. For data points with absolute values greater than S_{th} , we take the logarithm of the positive part directly. The negative part is first converted to its absolute value before being logarithmized, then taking the logarithm, and finally multiplying the negative sign back. The conversion formula is:

$$S_{i_log} = \begin{cases} S_{th} \log_{10}(S_i/S_{th}), & \text{for } S_i > S_{th}, \\ S_i, & \text{for } -S_{th} \leq S_i \leq S_{th}, \\ -S_{th} \log_{10}(-S_i/S_{th}), & \text{for } S_i < -S_{th}, \end{cases} \quad (i = 1, 2, 3, \dots, N) \quad (14)$$

where S_i is the value of each point in the spectrum we want to transform, and S_{i_log} is the spectrum after being logarithmized. N is the number of data points. S_{th} is some threshold value which defines the range of the transition part, and is set to $S_{th} = 1 \times 10^{-44}$ in this paper. This value is artificially selected. Any value is valid as long as its magnitude is smaller than most of the points in the target CSD; the smaller, the safer. The reason is described in the following paragraph.

It is established knowledge that the exponents of the spectrum points S_i with a base of 10 are negative. Here, for example, one of the point’s values $S_i = 10^{-30}$, and is a positive value in the “+” part. After taking logarithm directly (also base on 10), it comes to $\log_{10}(S_i) = -30$, which is a negative value. Obviously, the signs of each point after transforming are opposite to what was expected. A natural consideration is then simply multiplying them by -1 and reversing the signs. However, it is invalid because the relative magnitudes of the values are also inverted. To address this issue, before taking the logarithm of the data, we divide it by S_{th} , whose exponent is smaller than those of the “+” and “-” segments. Here as an example, $S_i/S_{th} = 10^{-30}/10^{-44} = 10^{14}$. This division transforms the exponents into positive numbers, without affecting the relative magnitudes of the original values. Finally, we multiply the logarithmic values by S_{th} ,

bringing all segments' magnitudes close to $\sim S_{\text{th}} = 10^{-44}$, which allows for smooth spline interpolation. Note that the transition part between the positive part and negative part, shown as the second line of Eq.(14), does not need any operation. Because its magnitude is so small that close to zero, thus has minimal impact on smooth interpolation.

Mathematically, S_{th} can be set to any value artificially. However, if it's so large that most of the points' magnitude is smaller than the threshold, the transition part will cover almost the whole frequency region, and no transformation will be done. Therefore, S_{th} should be a very small value, as we've talked about, smaller than most of the points in the target CSD. And obviously, the smaller the better.

3.4. Bayesian inference for spline coefficients

Starting from initial smooth curves, update the spline knots and trigonometric function coefficients utilizing the Markov Chain Monte Carlo (MCMC) sampling method [38] based on Bayesian inference to fit the noise auto-PSD and CSD. Crucially, the number of spline knots is dynamically updated via the trans-dimensional reversible jump MCMC (RJMCMC) method [39], enabling the program itself to adaptively fit the curve that describes the noise data best. This approach is similar to the **Bayeswave** method, while this paper considers the full noise covariance matrix when constructing the likelihood function:

$$\mathcal{L}(\mathbf{d}|\boldsymbol{\theta}) = \prod_f \frac{1}{\sqrt{(2\pi)^N |\mathbf{C}(f, \boldsymbol{\theta})|}} \exp\left(-\frac{1}{2} \mathbf{d}^\dagger(f) \mathbf{C}^{-1}(f, \boldsymbol{\theta}) \mathbf{d}(f)\right), \quad (15)$$

where $\boldsymbol{\theta}$ includes spline parameters for all auto-PSDs and CSDs, \mathbf{C} is the noise covariance matrix, and \mathbf{d} is residual data after subtracting GW signals and cleaning glitches, ideally only contains Gaussian stationary noise. Taking the logarithmic form and expanding the vectors, we have:

$$\log \mathcal{L} = -\frac{1}{2} \left[\begin{pmatrix} n_X^*(f) & n_Y^*(f) & n_Z^*(f) \end{pmatrix} \mathbf{C}^{-1} \begin{pmatrix} n_X(f) \\ n_Y(f) \\ n_Z(f) \end{pmatrix} + \log((2\pi)^N \det \mathbf{C}) \right] \quad (16)$$

where

$$\mathbf{C} = \begin{pmatrix} S_{XX}(f) & S_{XY}(f) & S_{XZ}(f) \\ S_{XY}^*(f) & S_{YY}(f) & S_{YZ}(f) \\ S_{XZ}^*(f) & S_{YZ}^*(f) & S_{ZZ}(f) \end{pmatrix} \quad (17)$$

Diagonal elements are the auto-PSDs, and off-diagonal elements are the CSDs we need to fit.

The prior distribution imposes upper and lower bounds on the number of knots and enforces relative smoothness at some connection points between spline interpolation and trigonometric function fitting (such that the difference is within an artificially preset range).

Theoretically, both the PSDs and CSDs are updated simultaneously during the RJMCMC process, and after sufficient iterations, the sampling chain will converge to

a stationary posterior distribution, where the likelihood function in the form of a multivariate Gaussian probability distribution jointly formed by the noise model and the input data reaches its maximum value. However, due to the combined influence of PSDs and CSDs on the computed value of the likelihood function, there may be situations where the two curves deviate significantly from theoretical expectations individually, yet the resulting posterior probability value is accepted. This reduces fitting efficiency and increases the number of iterations required to achieve convergence. To address this problem, referencing the **Gibbs** sampling methodology [40, 41], we decouple the fitting of each element in the **C** matrix. The main idea of **Gibbs** sampling is that, supposing the parameters can be clustered into distinct subsets $\Theta_1, \Theta_2, \Theta_3, \dots$, when updating a set of parameters Θ_1 , keep the other set of parameters $\Theta_2, \Theta_3, \dots$ fixed. Once the update of this iteration is complete, fix Θ_1 at its current optimal fitting position and proceed to update Θ_2 , and so on. Here, we illustrate a simplified scenario where $S_{XX} = S_{YY} = S_{ZZ}$, $S_{XY} = S_{XZ} = S_{YZ}$, implying that only one S_{XX} and one S_{XY} in the matrix require fitting.

The workflow of our method, shown in FIG.3 is as follows:

- 1) As described in Sec.3.1, 3.2, obtain the median-smoothed spectrum from data and select knots on it to perform spline interpolation. Near the two descent peaks in the high-frequency region, replace the interpolation curve with a trigonometric analytic expression, resulting in initial smooth curves $S_{XX\text{ini}}, S_{XY\text{ini}}$.
- 2) Fix CSD at current state (e.g. in the first iteration it's $S_{XY\text{ini}}$), independently fit S_{XX} . update the analytical expression coefficients, and perform a trans-dimensional update of the spline knots followed by re-interpolation, resulting in $S_{XX\text{fit}}$ after several iterations.
- 3) Fix PSD at $S_{XX\text{fit}}$, independently fit S_{XY} this time, and get $S_{XY\text{fit}}$.
- 4) Repeat step 2 and step 3 iteratively, and the final fitting results S_{XX}, S_{XY} are obtained.

Here in the **RJCMC** process, a crucial aspect is the criterion for determining whether to accept the proposed points each iteration. The typical acceptance ratio is calculated by:

$$\alpha(\theta_i, \theta^*) \equiv \min \left(1, \frac{P(\theta^* | D) q(\theta^* | \theta_i)}{P(\theta_i | D) q(\theta_i | \theta^*)} \right) \quad (18)$$

where θ_i, θ^* are the parameters of current state and proposed state, P is the posterior distribution and $q(\theta^* | \theta_i)$ is the proposal density from current state i to new state. Simply put, the algorithm always tends to accept states with higher posterior values, which in this study can translate to favoring higher likelihood. However, after several runs of the program, we observed that the knots located at the pronounced “concave” part (see $\sim 0.01\text{Hz}$ and $\sim 0.05\text{Hz}$) and “convex” part (see $\sim 0.03\text{Hz}$) of the PSD curve tend to be deleted during the trans-dimensional update process, especially the “concave”

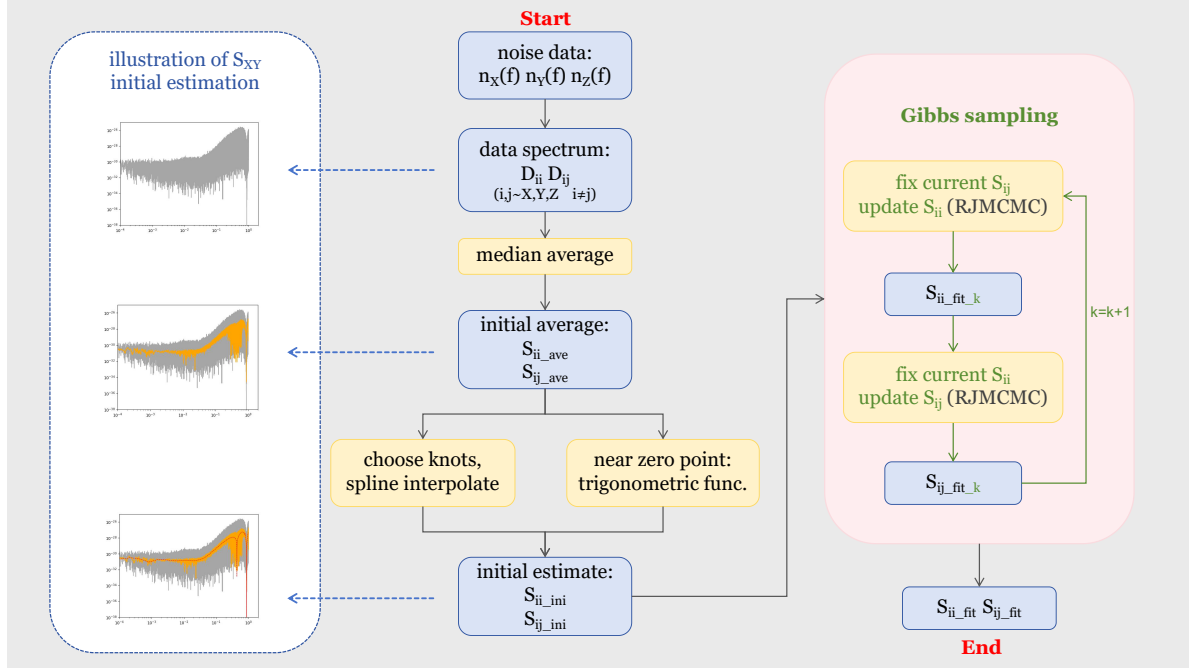


Figure 3: Flow diagram of the whole process of NOISAR. The process on the left side yields the initialized PSD and CSD, while the right side involves the trans-dimensional updating of PSD and CSD within the Gibbs framework.

ones. In that case, it becomes challenging to fit the fluctuating portions of the curve accurately.

This may be caused by two reasons:

1) The log-likelihood value is obtained by summing the values of each point in the frequency domain. Therefore, some points with higher values and some points with lower values may lead to a similar result, and the program tends to accept a simpler model with fewer concave and convex fluctuations.

2) To illustrate intuitively, the likelihood function shown as Eq. (16) can be written in a rough form: $-\mathbf{d}\mathbf{C}^{-1}\mathbf{d}^* - \log_term$. Data \mathbf{d} remains unchanged, so an increased value of \mathbf{C} would result in a larger likelihood value, which can be accepted by the program. When fitting PSD independently in step 2 described above, a higher curve compared with data would be selected. Though the log.term will restrict it from increasing unlimitedly, it's likely to choose a curve that is higher and has a simpler shape at the concave parts of the original curve.

To address this issue, we introduce an additional criterion for determining whether to accept the update: when the difference between the proposed point and current point is less than $3\sigma_{PSD}$, the update is accepted; otherwise, it is rejected. σ_{PSD} represents the variance of the spectrum obtained by averaging over the data spectrum. The derivation process for calculating σ_{PSD} is as follows.

Taking the auto-PSD as an example:

$$\text{PSD} = \frac{\sum_{i=j}^{j+m} \langle \tilde{n}_X(f) \tilde{n}_X^*(f') \rangle_i^2}{m} \quad (19)$$

where m represents the length over which an average is performed. To simplify the expression, let D_{sum} denote $\sum_{i=j}^{j+m} \langle \tilde{n}_X(f) \tilde{n}_X^*(f') \rangle_i^2$ we have:

$$\sigma_{\text{PSD}} = \frac{\sigma_{D_{\text{sum}}}}{m} \quad (20)$$

Since the data follows a Gaussian distribution with PSD as variance, $\frac{D_{\text{sum}}}{\text{PSD}}$ should follow a χ^2 distribution with m degrees of freedom, whose expected value is m and variance is $2m$. That is:

$$\sigma \left(\frac{D_{\text{sum}}}{\text{PSD}} \right) = \sqrt{2m} \quad (21)$$

In this equation, the denominator represents the theoretical PSD that the noise data satisfies, which is a constant. Therefore, it can be factored out of the parentheses. In practical scenarios, this PSD is unknown, we can substitute it with the initial PSD_0 obtained from Eq. (7). Combine Eq. (20) and Eq. (21), we have:

$$\sigma_{\text{PSD}} = \sqrt{\frac{2}{m}} \text{PSD}_0 \quad (22)$$

This additional acceptance criterion aims to restrict the updated spectrum from deviating too far from the initial spectrum. As previously mentioned, solely pursuing higher likelihoods and simpler curves would result in the loss of much of the information contained in the true spectrum. CSD fitting follows the same idea described above.

4. Implementation and Results

Taking the X and Y channels as an example, generate correlated noise using the full noise covariance matrix \mathbf{C} composed of the theoretical TianQin PSD and CSD. The observation duration is 10 days, with a sampling interval of 0.5 seconds. We consider Gaussian and stationary noise here as a preliminary proof-of-concept of the method. More complex scenarios including confusion noise, glitches and data gaps will be considered in the future improvements of NOISAR.

After a pre-processing phase, we get an initial smooth estimation of both diagonal and off-diagonal elements in matrix \mathbf{C} . Then run the RJMCMC process to update PSD_{fit} and CSD_{fit} in turn, each run for 1000 iterations, and each iteration takes approximately 1 second. Since our example is simple, we run only 2 circulations in Gibbs framework. The entire program can be completed in ~ 10 minutes using only one CPU core of the Xeon Gold 6330 type.

FIG. 4 shows the PSD recovered by NOISAR (dashed black) compared with the theoretical PSD (solid red) of X channel on a logarithmic coordinate system. As can be seen from the figure, our method can recover the fluctuations of the PSD curve in the low-frequency region and the descending peak in the high-frequency region. FIG. 5

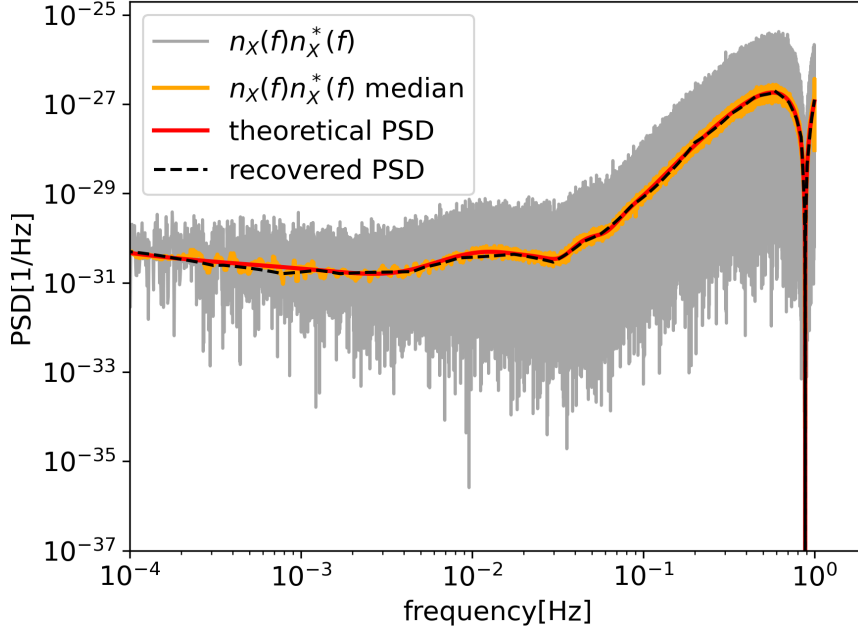


Figure 4: Recovered PSD (dashed black) compared with theoretical PSD (solid red) of X channel on a logarithmic coordinate system. The grey line shows the auto-correlated data spectrum, which is the noise in the X channel multiplied by its complex conjugate. The orange line is the median smoothed spectrum.

shows the results of CSD fitting. The upper panel shows the cross-correlated data spectrum and CSD with absolute values taken. To demonstrate the characteristic of the CSD having both positive and negative values, as well as the software's performance in the negative region, the bottom panel displays the log-transformed data spectrum and CSD curve, using the log method described in Sec. 3.3. It can be observed that our method can accurately restore the feature of the cross-correlated spectrum transitioning from negative to positive values and descending back to zero. We also calculate the relative error between the recovered spectrum S_{rec} and the theoretical one S_{theo} , which is $|(S_{rec} - S_{theo})/S_{theo}|$. Both PSD and CSD are estimated with an averaged error $\leq 10\%$ in the whole frequency region.

5. Discussion and conclusion

This paper advances noise modeling for multi-channel systems, considers a full noise covariance matrix whose off-elements are not ignored, and develops a software **NOISAR** for adaptive modeling of noise covariance in space-based gravitational wave detectors. We employ a semi-analytical noise modeling approach, using spline interpolation to fit the low-frequency portion of the spectrum, and the trigonometric function to capture the high-frequency features that descend to zero or cross through zero. The initial estimated

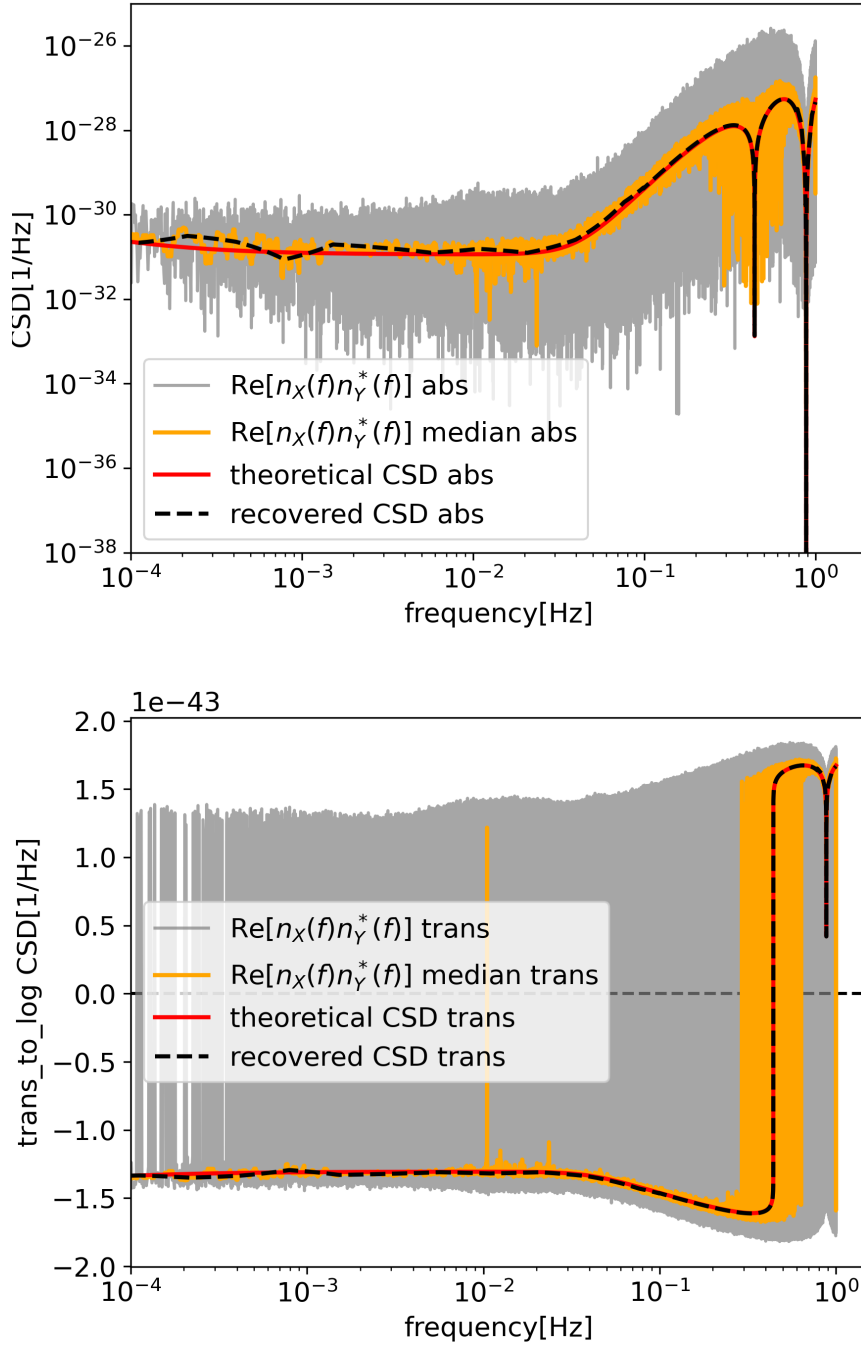


Figure 5: Recovered CSD (dashed black) compared with theoretical CSD (solid red) of XY channel. The grey line shows the cross-correlated data spectrum, which is the noise in the X channel multiplied by the complex conjugate of the noise in the Y channel. The orange line is the median smoothed spectrum. The upper panel displays the result after taking the absolute value. The bottom panel shows the log-transformed result in both positive and negative regions.

spectrum is derived solely from smoothing the noise data spectrum. Then update it using trans-dimensional Bayesian inference. The entire process is phenomenological and does not require prior knowledge of the noise model.

In this paper, we implement the preliminary version of NOISAR in a simple scenario: the PSDs of the X , Y , and Z channels are equal, and the CSDs between them are also the same. We consider the case of pure Gaussian noise. Using **NOISAR** we can effectively recover the features of both auto- and cross-spectrum densities, with the overall relative error smaller than 10% compared with the injected theoretical ones.

Since this method is flexible and does not rely on prior models, it applies to more complex scenarios as well. If we consider the case where the noise in X, Y, Z channels are not identical, all nine elements in the noise covariance matrix are treated as parameters to be fitted, while the method remains the same as when there are only two parameters (S_{XX} and S_{XY}). In this case, we may need to make efforts in computational acceleration because the dimension of the parameter space has increased severalfold (from 2 to 9). Besides, since the method is phenomenological, if the data contains some residual due to inaccurate parameter estimation and GW signal subtraction, it would be treated as part of the noise and fitted into the noise covariance matrix within this program. In the data analysis pipeline where noise and signals are iteratively fitted (e.g., global fit), this may not be a problem because the large amount of updates in the program will gradually refine the modeling of both noise and signal using the **Gibbs** sampling framework. In the initial several iterations, the signal parameter estimation and noise modeling results may not be ideal. However, each module's updated output progressively improves the performance of other modules. This iterative refinement cycle ultimately yields satisfactory recovery for both signal parameters and noise.

For future work, we will consider more complex conditions, including non-stationary noise such as glitches, data gaps in the data stream, to make this software more universal and applicable to real detected gravitational wave data analysis. This software can be combined into the global fit pipeline for space-based gravitational wave detectors, as a noise modeling block, to give a full noise covariance matrix in the likelihood calculation for the GW parameter estimation.

Acknowledgments

This work has been supported in part by the National Key Research and Development Program of China (No. 2023YFC2206700). YMH is also supported by the Natural Science Foundation of China (Grants No. 12173104, and No. 12261131504), and the science research grants from the China Manned Space Project.

References

- [1] Daniel Sigg and (for the LIGO Science Collaboration). Status of the ligo detectors. *Classical and Quantum Gravity*, 23(8):S51, mar 2006.

- [2] The VIRGO Collaboration; F Acernese, P Amico, N Arnaud, D Babusci, G Ballardin, R Barillé, F Barone, M Barsuglia, F Beauville, F Bellachia, M A Bizouard, C Boccara, D Boget, F Bondu, C Bourgoïn, A Bozzi, S Braccini, C Bradaschia, A Brillet, V Brisson, L Brocco, D Buskulic, J Cachenaut, G Calamai, E Calloni, E Campagna, C Casciano, C Cattuto, F Cavalier, S Cavaliere, R Cavalieri, G Cella, E Chassande-Mottin, F Chollet, F Cleva, T Cokelaer, G Conforto, S Cortese, J P Coulon, E Cuoco, V Dattilo, P Y David, M Davier, M De Rosa, R De Rosa, L Di Fiore, A Di Virgilio, B Dujardin, P Dominici, A Eleuteri, D Enard, G Evangelista, I Ferrante, F Fidecaro, I Fiori, R Flaminio, D Forest, J D Fournier, L Fournier, S Frasca, F Frasconi, L Gammaitoni, P Ganau, A Gennai, G Gennaro, L Giacobone, A Giazotto, G Giordano, C Girard, G Gougoulat, G M Guidi, H Heitmann, P Hello, R Hermel, P Heusse, L Holloway, F Honglie, M Iannarelli, L Journet, S Krecklbergh, B Lagrange, P La Penna, M Leliboux, B Lieunard, T Lomtadze, V Lorette, G Losurdo, M Loupias, J M Mackowski, E Majorana, C N Man, F Marchesoni, F Marion, F Martelli, A Masserot, L Massonnet, S Mataguez, F Menzinger, M Mazzoni, C Michel, L Milano, J L Montorio, F Moreau, J Moreau, N Morgado, F Mornet, B Mours, P Mugnier, F Nenci, J Pacheco, A Pai, C Palomba, F Paoletti, A Paoli, L Paoli, A Pasqualetti, R Passaquieti, D Passuello, M Perciballi, S Peruzzi, B Perniola, L Pinard, R Poggiani, P Popolizio, E Porter, S Puccinelli, M Punturo, P Puppo, K Qipiani, J Ramonet, P Rapagnani, V Reita, A Remillieux, F Ricci, F Richard, J P Roger, P Ruggi, G Russo, S Solimeno, R Stanga, R Taddei, J M Teuler, E Tournefier, F Travasso, H Trinquet, E Turri, M Varvella, D Verkindt, F Vetrano, O Veziant, A Viceré, S Vilalte, J Y Vinet, H Vocca, M Yvert, and Z Zhang. Status of virgo. *Classical and Quantum Gravity*, 20(17):S609, aug 2003.
- [3] Kentaro Somiya and (for the KAGRA Collaboration). Detector configuration of kagra—the japanese cryogenic gravitational-wave detector. *Classical and Quantum Gravity*, 29(12):124007, jun 2012.
- [4] Jianwei Mei, Yan-Zheng Bai, et al. The tianqin project: Current progress on science and technology. *Progress of Theoretical and Experimental Physics*, 2021(5):05A107, 2021.
- [5] J. Luo, L. S. Chen, H. Z. Duan, Y. G. Gong, S. Hu, J. Ji, Q. Liu, J. Mei, V. Milyukov, and M. Sazhin. Tianqin: a space-borne gravitational wave detector. *Classical & Quantum Gravity*, 33(3):035010, 2015.
- [6] Karsten Danzmann and the LISA study team. Lisa: laser interferometer space antenna for gravitational wave measurements. *Classical and Quantum Gravity*, 13(11A):A247, nov 1996.
- [7] David Cyranoski. Chinese gravitational-wave hunt hits crunch time. *Nature*, 531:150–151, 2016.
- [8] En-Kun Li et al. Gravitational Wave Astronomy With TianQin. 9 2024.
- [9] Stanislav Babak, Antoine Petiteau, and Martin Hewitson. LISA Sensitivity and SNR Calculations. 8 2021.
- [10] P. L. Bender. Wavefront distortion and beam pointing for LISA. *Class. Quant. Grav.*, 22:S339–S346, 2005.
- [11] J. W. Armstrong, F. B. Estabrook, and Massimo Tinto. Time-delay interferometry for space-based gravitational wave searches. *The Astrophysical Journal*, 527(2):814, dec 1999.
- [12] Massimo Tinto, F. B. Estabrook, and J. W. Armstrong. Time delay interferometry for LISA. *Phys. Rev. D*, 65:082003, 2002.
- [13] F. B. Estabrook, Massimo Tinto, and J. W. Armstrong. Time delay analysis of LISA gravitational wave data: Elimination of spacecraft motion effects. *Phys. Rev. D*, 62:042002, 2000.
- [14] Tania Regimbau. The astrophysical gravitational wave stochastic background. *Res. Astron. Astrophys.*, 11:369–390, 2011.
- [15] Michele Maggiore. *Gravitational Waves. Vol. 2: Astrophysics and Cosmology*. Oxford University Press, 3 2018.
- [16] Nelson Christensen. Stochastic gravitational wave backgrounds. *Reports on Progress in Physics*, 82(1):016903, nov 2018.
- [17] Jun Cheng, En-Kun Li, Yi-Ming Hu, Zheng-Cheng Liang, Jian-dong Zhang, and Jianwei Mei. Detecting the stochastic gravitational wave background with the TianQin detector. *Phys. Rev.*

- D*, 106(12):124027, 2022.
- [18] Valeriya Korol, Elena M. Rossi, and Enrico Barausse. A multimessenger study of the Milky Way’s stellar disc and bulge with LISA, Gaia, and LSST. *Mon. Not. Roy. Astron. Soc.*, 483(4):5518–5533, 2019.
 - [19] Matthew R. Adams, Neil J. Cornish, and Tyson B. Littenberg. Astrophysical Model Selection in Gravitational Wave Astronomy. *Phys. Rev. D*, 86:124032, 2012.
 - [20] Tyson B. Littenberg and Neil J. Cornish. Prototype global analysis of LISA data with multiple source types. *Phys. Rev. D*, 107(6):063004, 2023.
 - [21] Stefan H. Strub, Luigi Ferraioli, Cédric Schmelzbach, Simon C. Stähler, and Domenico Giardini. Global Analysis of LISA Data with Galactic Binaries and Massive Black Hole Binaries. 3 2024.
 - [22] Michael L. Katz, Nikolaos Karnesis, Natalia Korsakova, Jonathan R. Gair, and Nikolaos Stergioulas. An efficient GPU-accelerated multi-source global fit pipeline for LISA data analysis. 5 2024.
 - [23] Senwen Deng, Stanislav Babak, Maude Le Jeune, Sylvain Marsat, Éric Plagnol, and Andrea Sartirana. Modular global-fit pipeline for LISA data analysis. 1 2025.
 - [24] Matthew R. Adams and Neil J. Cornish. Discriminating between a Stochastic Gravitational Wave Background and Instrument Noise. *Phys. Rev. D*, 82:022002, 2010.
 - [25] Quentin Baghi, Nikolaos Karnesis, Jean-Baptiste Bayle, Marc Besançon, and Henri Inchauspé. Uncovering gravitational-wave backgrounds from noises of unknown shape with LISA. *JCAP*, 04:066, 2023.
 - [26] Ilaria Caporali, Giulia Capurri, Walter Del Pozzo, Angelo Ricciardone, and Lorenzo Valbusa Dall’Armi. Impact of correlated noise on the reconstruction of the stochastic gravitational wave background with Einstein Telescope. 1 2025.
 - [27] M. Punturo et al. The Einstein Telescope: A third-generation gravitational wave observatory. *Class. Quant. Grav.*, 27:194002, 2010.
 - [28] Michele Maggiore et al. Science Case for the Einstein Telescope. *JCAP*, 03:050, 2020.
 - [29] P. Welch. The use of fast Fourier transform for the estimation of power spectra: A method based on time averaging over short, modified periodograms. *IEEE Trans. Audio Electroacoust.*, 15(2):70–73, 1967.
 - [30] Katerina Chatziioannou, Carl-Johan Haster, Tyson B. Littenberg, Will M. Farr, Sudarshan Ghonge, Margaret Millhouse, James A. Clark, and Neil Cornish. Noise spectral estimation methods and their impact on gravitational wave measurement of compact binary mergers. *Phys. Rev. D*, 100(10):104004, 2019.
 - [31] Christian Rover, Renate Meyer, and Nelson Christensen. Modelling coloured residual noise in gravitational-wave signal processing. *Class. Quant. Grav.*, 28:015010, 2011.
 - [32] Colm Talbot and Eric Thrane. Gravitational-wave astronomy with an uncertain noise power spectral density. *Phys. Rev. Res.*, 2(4):043298, 2020.
 - [33] Tyson B. Littenberg and Neil J. Cornish. Bayesian inference for spectral estimation of gravitational wave detector noise. *Phys. Rev. D*, 91(8):084034, 2015.
 - [34] Neil J. Cornish and Tyson B. Littenberg. BayesWave: Bayesian Inference for Gravitational Wave Bursts and Instrument Glitches. *Class. Quant. Grav.*, 32(13):135012, 2015.
 - [35] Neil J. Cornish, Tyson B. Littenberg, Bence Bécsy, Katerina Chatziioannou, James A. Clark, Sudarshan Ghonge, and Margaret Millhouse. BayesWave analysis pipeline in the era of gravitational wave observations. *Phys. Rev. D*, 103(4):044006, 2021.
 - [36] Bence Bécsy, Peter Raffai, Neil J. Cornish, Reed Essick, Jonah Kanner, Erik Katsavounidis, Tyson B. Littenberg, Margaret Millhouse, and Salvatore Vitale. Parameter estimation for gravitational-wave bursts with the BayesWave pipeline. *Astrophys. J.*, 839(1):15, 2017.
 - [37] Toral Gupta and Neil J. Cornish. Bayesian power spectral estimation of gravitational wave detector noise revisited. *Phys. Rev. D*, 109(6):064040, 2024.
 - [38] W. K. Hastings. Monte carlo sampling methods using markov chains and their applications. *Biometrika*, 57(1):97–109, 1970.

- [39] PETER J. GREEN. Reversible jump Markov chain Monte Carlo computation and Bayesian model determination. *Biometrika*, 82(4):711–732, 12 1995.
- [40] Christian Ritter and Martin A. Tanner. Facilitating the gibbs sampler: The gibbs stopper and the griddy-gibbs sampler. *Journal of the American Statistical Association*, 87(419):861–868, 1992.
- [41] W. R. Gilks and P. Wild. Adaptive rejection sampling for gibbs sampling. *Journal of the Royal Statistical Society. Series C (Applied Statistics)*, 41(2):337–348, 1992.